INTERNATIONAL JOURNAL FOR NUMERICAL METHODS IN FLUIDS
Int. J. Numer. Meth. Fluids 2002; **39**:247–275 (DOI: 10.1002/fld.285)

A numerical model for the flooding and drying of irregular domains

P. Brufau[1,*], M. E. Vázquez-Cendón[2] and P. García-Navarro[1]

[1]*Fluid Mechanics, Centro Politécnico Superior, University of Zaragoza, Spain*
[2]*Applied Mathematics, University of Santiago de Compostela, Spain*

SUMMARY

A numerical technique for the modelling of shallow water flow in one and two dimensions is presented in this work along with the results obtained in different applications involving unsteady flows in complex geometries. A cell-centred finite volume method based on Roe's approximate Riemann solver across the edges of both structured and unstructured cells is presented. The discretization of the bed slope source terms is done following an upwind approach. In some applications a problem arises when the flow propagates over adverse dry bed slopes, so a special procedure has been introduced to model the advancing front. It is shown that this modification reproduces exactly steady state of still water in configurations with strong variations in bed slope and contour. The applications presented are mainly related with unsteady flow problems. The scheme is capable of handling complex flow domains as will be shown in the simulations corresponding to the test cases that are going to be presented. Comparisons of experimental and numerical results are shown for some of the tests. Copyright © 2002 John Wiley & Sons, Ltd.

KEY WORDS: unsteady flow; complex flow domains; irregular domains; flooding; drying

1. INTRODUCTION

Many efforts have been recently devoted to the development of numerical techniques for free surface flows. Among them, those oriented to the resolution of unsteady shallow water flow have been strongly influenced by the upwind philosophy initially introduced in Gas Dynamics. These methods are specially suited for advection dominated problems and their implementation is not straightforward when source terms are relevant so that the bed variations terms are as important as advection terms [1, 2].

There has been much research in CFD into the efficient solution of homogeneous systems of conservation laws. The main focus has been put on the accurate representation of sharp discontinuities such as shock waves in gases or hydraulic jumps in shallow flows. More recently, as numerical models become more complicated and the areas of application of these

*Correspondence to: P. Brufau, Fluid Mechanics, Centro Politécnico Superior, University of Zaragoza, Maria de Luna 3, 50018 Zaragoza, Spain.

Received February 2001
Revised October 2001

methods grow, it has become important that other aspects of the discretization be given due attention. This is certainly true in the field of computational hydraulics where the modelling can be dominated by the effects not only of source terms, but also of the propagation over an initially dry and irregular bed.

The shallow water or St.Venant equations [3] are accepted for many practical applications as properly modelling the unsteady flow of water either in a one- or a two-dimensional approach. They are the differential form of the conservation of mass and momentum [4]. There exist methods that have been developed to deal with the Euler equations that are able to cope with complex systems of discontinuities and shock waves [5–8]. It is well known that the non-linearity of the hyperbolic shallow water equations may render their solution complicated, in the sense of giving rise to the appearance of discontinuities, which reflect physical phenomena such as hydraulic jumps and surges. New schemes have been reported successful for flow in channels [9, 10]. However, their application to river flow and complex geometries is not so common in the literature [11]. The presence of extreme slopes, high roughness and strong changes in the irregular geometry represent a great difficulty that can lead to important numerical errors presumably arising from the source terms of the equations [1, 12]. The importance of the numerical discretization of these terms makes the interest of increasing the order of accuracy of the basic advective scheme sometimes doubtful. This is greater when the problem involves propagation over irregular dry beds.

In this work, a first-order advection scheme is adopted. It is a well known Godunov-type scheme based on Roe's approximate Riemann solver. For the sake of clarity, the governing equations are first recalled in Section 2 and the main features of the method are outlined in Section 3. Section 4 is devoted to the discussion of the discretization at the domain boundaries, distinguishing between fixed and moving boundaries (wetting/drying fronts). The examples presented in Section 5 are divided in one- and two-dimensional cases. They all show the performance of the proposed technique.

2. GOVERNING EQUATIONS

2.1. 2D mathematical model

The two-dimensional shallow water equations, which represent mass and momentum conservation in plane, can be obtained by depth averaging the Navier–Stokes equations. Neglecting diffusion of momentum due to viscosity and turbulence, wind effects and the Coriolis term, they form the following system of equations:

$$\frac{\partial \mathbf{U}}{\partial t} + \frac{\partial \mathbf{F}}{\partial x}(\mathbf{U}) + \frac{\partial \mathbf{G}}{\partial y}(\mathbf{U}) = \mathbf{S}(x, y, \mathbf{U}) \tag{1}$$

in which,

$$\mathbf{U} = (h, q_x, q_y)^T$$

$$\mathbf{F} = \left(q_x, \frac{q_x^2}{h} + \frac{gh^2}{2}, \frac{q_x q_y}{h} \right)^T$$

$$\mathbf{G} = \left(q_y, \frac{q_x q_y}{h}, \frac{q_y^2}{h} + \frac{gh^2}{2} \right)^T$$

where $q_x = uh$ and $q_y = vh$. The variable h represents the water depth, g is the acceleration of the gravity and (u, v) are the depth averaged components of the velocity $\mathbf{u}$ along the x and y coordinates respectively. The source terms in the momentum equation are the bed slopes and the friction losses along the two coordinate directions,

$$\mathbf{S} = (0, gh(S_{0x} - S_{fx}), gh(S_{0y} - S_{fy}))^T$$

where,

$$S_{0x} = -\frac{\partial z}{\partial x}, \quad S_{0y} = -\frac{\partial z}{\partial y}$$

and the friction losses in terms of the Manning's roughness coefficient [13]. It is useful to rewrite Equation (1)

$$\frac{\partial \mathbf{U}}{\partial t} + \boldsymbol{\nabla} \cdot \mathbf{E}(\mathbf{U}) = \mathbf{S}(x, y, \mathbf{U}) \tag{2}$$

in which $\mathbf{E} = (\mathbf{F}, \mathbf{G})^T$, since this displays the conservative character of the system in the absence of source terms, and also in order to introduce the integral form of the equations over a fixed volume Ω,

$$\frac{\partial}{\partial t} \int_\Omega \mathbf{U} \, \mathrm{d}\Omega + \int_\Omega (\boldsymbol{\nabla} \cdot \mathbf{E}) \, \mathrm{d}\Omega = \int_\Omega \mathbf{S} \, \mathrm{d}\Omega \tag{3}$$

This form of the equations of motion is more general and anticipates the finite volume technique of discretization that will be applied. The application of Gauss's theorem to the flux integral allows us to rewrite it as

$$\frac{\partial}{\partial t} \int_\Omega \mathbf{U} \, \mathrm{d}\Omega + \oint_{\partial\Omega} (\mathbf{E} \cdot \mathbf{n}) \, \mathrm{d}s = \int_\Omega \mathbf{S} \, \mathrm{d}\Omega \tag{4}$$

where $\partial\Omega$ denotes the surface surrounding the volume Ω and $\mathbf{n}$ is the unit outward normal vector.

A cell-centred finite volume method will be formulated over a control volume where the dependent variables of the system are represented as piecewise constants. In the two-dimensional approach presented in this work, the spatial domain of integration is covered by a set of quadrilateral or triangular cells, not necessarily aligned with the coordinate directions. A discrete approximation to Equation (4) is applied in every cell Ω_i so that the volume integrals represent integrals over the area of the cell and the surface integrals represent the total flux through the cell boundaries. Denoting by $\mathbf{U}_i$ the average value of the conservative variables over the volume Ω_i at a given time, from Equation (4) the following conservation equation can be written for every cell:

$$\frac{\partial \mathbf{U}_i}{\partial t} A_i + \oint_{\partial\Omega_i} (\mathbf{E} \cdot \mathbf{n}) \, \mathrm{d}s = \int_\Omega \mathbf{S} \, \mathrm{d}\Omega \tag{5}$$

where A_i is the area of the cell Ω_i.

The Jacobian matrix, $\mathbf{J_n}$, of the normal flux $(\mathbf{E}\cdot\mathbf{n})$ is evaluated as

$$\mathbf{J_n}=\frac{\partial(\mathbf{E}\cdot\mathbf{n})}{\partial\mathbf{U}}=\frac{\partial\mathbf{F}}{\partial\mathbf{U}}n_x+\frac{\partial\mathbf{G}}{\partial\mathbf{U}}n_y$$

and can be expressed as

$$\mathbf{J_n}=\begin{pmatrix} 0 & n_x & n_y \\ (gh-\frac{q_x^2}{h^2})n_x-\frac{q_xq_y}{h^2}n_y & \frac{q_y}{h}n_y+\frac{2q_x}{h}n_x & \frac{q_x}{h}n_y \\ (gh-\frac{q_y^2}{h^2})n_y-\frac{q_xq_y}{h^2}n_x & \frac{q_y}{h}n_x & \frac{q_x}{h}n_x+\frac{2q_y}{h}n_y \end{pmatrix}$$

The eigenvalues of $\mathbf{J_n}$ are a representation of the characteristic speeds

$$\begin{aligned}\lambda^1&=un_x+vn_y+c\\ \lambda^2&=un_x+vn_y\\ \lambda^3&=un_x+vn_y-c\end{aligned}\tag{6}$$

where $c=\sqrt{gh}$ is the celerity of the small amplitude surface waves.

The corresponding eigenvectors are

$$\mathbf{e}^1=\begin{pmatrix}1\\ u+cn_x\\ v+cn_y\end{pmatrix},\quad \mathbf{e}^2=\begin{pmatrix}0\\ -cn_y\\ cn_x\end{pmatrix},\quad \mathbf{e}^3=\begin{pmatrix}1\\ u-cn_x\\ v-cn_y\end{pmatrix}\tag{7}$$

From its eigenvectors, two matrices $\mathbf{P}$ and $\mathbf{P}^{-1}$ can be constructed with the property that they diagonalize the Jacobian $\mathbf{J_n}$.

$$\mathbf{J_n}=\mathbf{P}\boldsymbol{\Lambda}\mathbf{P}^{-1}$$

where $\boldsymbol{\Lambda}$ is a diagonal matrix with eigenvalues in the main diagonal.

2.2. 1D mathematical model

Many hydraulic situations can be described by means of a one-dimensional model, usually because a more detailed resolution is unnecessary. The equations governing the one-dimensional model can be derived by simple suppression of the y components from Equation (1). This, however, leads to a formulation containing only information per unit width, thus only valid for simple cases. If a more general one-dimensional model is sought in which the full geometry is retained, a second average on the width is required. Alternatively, the one-dimensional formulation can be derived from mass and momentum control volume analysis [4]. The 1D equations to model unsteady flow in a channel of variable breadth and depth can then be written in the form:

$$\frac{\partial\mathbf{U}}{\partial t}+\frac{\partial\mathbf{F}}{\partial x}(x,\mathbf{U})=\mathbf{S}(x,\mathbf{U})\tag{8}$$

with

$$\mathbf{U} = (A, Q)^T$$

$$\mathbf{F} = \left(Q, \frac{Q^2}{A} + gI_1\right)^T \tag{9}$$

$$\mathbf{S} = (0, gI_2 + gA(S_0 - S_f))^T$$

In Equation (9), A is the wetted cross-sectional area, Q is the discharge and I_1 represents a cross-sectional hydrostatic pressure force term

$$I_1 = \int_0^{h(x,t)} (h - \eta) b(x, \eta)\, \mathrm{d}\eta$$

in terms of the surface water level $h(x,t)$ and the breadth:

$$b(x, \eta) = \frac{\partial A(x,t)}{\partial \eta}$$

The pressure forces can have a component in the direction of the main stream (gI_2) due to the reaction of the walls in case of variations in shape along this direction. The amount of this force depends on the cross-sectional variation for constant depth. It is important to note that the validity of this approach is linked to the hypothesis of gradual variation. If sudden expansions or contractions take place, the approach is not valid.

The mass force is the projection of the weight of the volume of water in the direction of the stream. The bed slope is the derivative of the bottom elevation z and defines S_0,

$$S_0 = -\frac{\partial z(x)}{\partial x}$$

The friction term represents the action of the shear between the fluid and the solid walls. S_f stands for the energy grade line and is defined, for example, in terms of the Manning's roughness coefficient n [13].

In those cases in which $\mathbf{F} = \mathbf{F}(\mathbf{U})$ it is possible to rewrite the conservative system in the form

$$\frac{\partial \mathbf{U}}{\partial t} + \mathbf{J}\frac{\partial \mathbf{U}}{\partial x} = \mathbf{S}(x, \mathbf{U}) \tag{10}$$

The Jacobian matrix of the system (10) is

$$\mathbf{J} = \frac{\partial \mathbf{F}}{\partial \mathbf{U}} = \begin{pmatrix} 0 & 1 \\ c^2 - u^2 & 2u \end{pmatrix}$$

where $u = Q/A$ is the cross-section averaged water velocity and $c = \sqrt{gA/b}$. The eigenvalues and eigenvectors of $\mathbf{J}$ are:

$$\lambda^{1,2} = u \pm c$$

$$\mathbf{e}^{1,2} = (1, u \pm c)^T$$

This form of the equations is particularly useful in the context of upwind schemes. Other situations in which $\mathbf{F}=\mathbf{F}(\mathbf{U},x)$ are studied in García-Navarro and Vázquez-Cendón [14] and Hubbard and García-Navarro [15].

3. NUMERICAL METHOD

Upwind schemes are based on the idea of discretizing the spatial derivatives so that information is taken from the side it comes. Hence, a sense of propagation is implied and these techniques are well adapted to advection dominated problems. When source terms are present, it has previously been shown [1, 2, 14–16] that the flux derivatives and the source terms have to be discretized in a similar manner. The evaluation of fluxes and sources at the same local state is important.

The finite volume procedure defined in Section 2 is completely general. A mesh fixed in time is assumed and the contour integral is approached via a mid-point rule, i.e., a numerical flux is defined at the mid-point of each edge, giving

$$\oint_{\partial\Omega_i}(\mathbf{E}\cdot\mathbf{n})\,\mathrm{d}s\approx\sum_{k=1}^{NE}(\mathbf{E}_k^*\cdot\mathbf{n}_k)\,\mathrm{d}s_k \tag{11}$$

where k represents the edge index of the cell Ω_i, NE is the total number of edges in the cell ($NE=3$ for triangles, $NE=4$ for quadrilaterals). The vector $\mathbf{n}_k$ is the unit outward normal, $\mathrm{d}s_k$ is the length of the side, and $\mathbf{E}_k^*=(\mathbf{F},\mathbf{G})_k^*$ is the numerical flux tensor. Different implementations arise depending on the numerical scheme used and, consequently, on the numerical flux $\mathbf{E}^*$. The technique is outlined for a 2D domain. 1D developments follow the same line taking into account that in that case the outward normal $\mathbf{n}$ can have only the positive and negative senses of the axis ($NE=2$).

The evaluation of the numerical flux used in this work is based on the Riemann problem defined by the conditions on the left and right sides of the cell edges. A 1D philosophy is followed along the normal direction to the cell walls, making use of the normal numerical fluxes. The definition of an approximated flux Jacobian, $\tilde{\mathbf{J}}_{RL}$, constructed at the edges of the cells is exploited here. Once this matrix has been defined, the numerical flux across each edge k of the computational cells Ω_L on the left and Ω_R on the right in a 2D domain is [17]

$$(\mathbf{F},\mathbf{G})^*\cdot\mathbf{n}=\frac{1}{2}[(\mathbf{F},\mathbf{G})_R\cdot\mathbf{n}+(\mathbf{F},\mathbf{G})_L\cdot\mathbf{n}-|\tilde{\mathbf{J}}_{RL}|(\mathbf{U}_R-\mathbf{U}_L)] \tag{12}$$

Note that subscript k will be omitted for the sake of clarity and the following discussion is referred to the cell side k. As suggested by Roe [8] the matrix $\tilde{\mathbf{J}}_{RL}$ has the same shape as $\mathbf{J}_\mathbf{n}$ but is evaluated at an average state given by the quantities $\tilde{\mathbf{u}}=(\tilde{u},\tilde{v})$ and $\tilde{c}$ which must be calculated according to the matrix properties [17]:

1. $\tilde{\mathbf{J}}_{RL}=\tilde{\mathbf{J}}_{RL}(\mathbf{U}_R,\mathbf{U}_L)$.
2. $\mathbf{F}_R-\mathbf{F}_L=\tilde{\mathbf{J}}_{RL}(\mathbf{U}_R-\mathbf{U}_L)$.
3. $\tilde{\mathbf{J}}_{RL}$ has a complete set of real and different eigenvalues and eigenvectors.
4. $\tilde{\mathbf{J}}_{RL}(\mathbf{U}_L,\mathbf{U}_L)=\mathbf{J}_\mathbf{n}(\mathbf{U}_L)$.

The approximate Jacobian matrix is not directly used in the actual method. Instead, the difference in the vector $\mathbf{U}$ across the grid edge is decomposed on the matrix eigenvectors basis as

$$\Delta\mathbf{U} = \mathbf{U}_R - \mathbf{U}_L = \sum_{m=1}^{3} \alpha^m \mathbf{e}^m \tag{13}$$

where the expression of coefficients α^m are [17]:

$$\begin{aligned} \alpha^{1,3} &= \frac{h_R - h_L}{2} \pm \frac{1}{2\tilde{c}}[((hu)_R - (hu)_L)n_x + ((hv)_R - (hv)_L)n_y - (\tilde{u}n_x + \tilde{v}n_y)(h_R - h_L)] \\ \alpha^2 &= \frac{1}{\tilde{c}}[((hv)_R - (hv)_L - \tilde{v}(h_R - h_L))n_x - ((hv)_R - (hv)_L - \tilde{u}(h_R - h_L))n_y] \end{aligned} \tag{14}$$

Matrix $|\tilde{\mathbf{J}}_{RL}|$ is replaced by its eigenvalues and eigenvectors in the product $|\tilde{\mathbf{J}}_{RL}|(\mathbf{U}_R - \mathbf{U}_L)$ in the form

$$|\tilde{\mathbf{J}}_{RL}|(\mathbf{U}_R - \mathbf{U}_L) = \sum_{m=1}^{3} |\tilde{\lambda}^m| \alpha^m \tilde{\mathbf{e}}^m \tag{15}$$

From the eigenvalues of $\mathbf{J}$, those of $\tilde{\mathbf{J}}_{RL}$ have the form of Equation (6) and the eigenvectors have the form of Equation (7), all in terms of average velocities and celerity. Enforcing the second condition [17] of the matrix $\tilde{\mathbf{J}}_{RL}$ the following expressions for $\tilde{u}, \tilde{v}$ and $\tilde{c}$ can be obtained

$$\tilde{u} = \frac{\sqrt{h_R}u_R + \sqrt{h_L}u_L}{\sqrt{h_R} + \sqrt{h_L}}, \quad \tilde{v} = \frac{\sqrt{h_R}v_R + \sqrt{h_L}v_L}{\sqrt{h_R} + \sqrt{h_L}}, \quad \tilde{c} = \sqrt{\frac{g}{2}(h_R + h_L)} \tag{16}$$

It has to be stressed at this point that in case of an advancing front over dry bed the average velocities are calculated in the form

$$\tilde{u} = \frac{u_R + u_L}{2}, \quad \tilde{v} = \frac{v_R + v_L}{2} \tag{17}$$

because the velocity values at the right or left cell are zero. This election is proposed by the Q-scheme of Van Leer [12] for this situation. For example, if the right cell is a dry cell, Equation (16) gives

$$\tilde{u} = u_L, \quad \tilde{v} = v_L \tag{18}$$

and the front would advance with the total velocity of the wet cell instead of its average value. However, the average value for the celerity is calculated always in the same form, otherwise the balance between the flux and the bed slope is not achieved in steady flow leading to numerical errors (see Section 4.2).

Expression (12) provides the numerical flux normal to each edge of the computational so that Equation (5) becomes

$$\mathbf{U}_i^{n+1} = \mathbf{U}_i^n - \frac{\Delta t}{A_i}\left(\sum_{k=1}^{NE} \mathbf{E}_k^* \cdot \mathbf{n}_k \, \mathrm{d}s_k\right)_i^n + \Delta t \int_\Omega \mathbf{S} \, \mathrm{d}\Omega \tag{19}$$

This form of updating the variables via a numerical interface flux is common in finite volume methods. It is less common, but also possible, to re-express Equation (19) in a different form by realizing that

$$\Delta(\mathbf{E}\cdot\mathbf{n}) = \tilde{\mathbf{J}}_{RL}\Delta\mathbf{U} = \tilde{\mathbf{P}}\tilde{\mathbf{\Lambda}}\tilde{\mathbf{P}}^{-1}\Delta\mathbf{U} = \tilde{\mathbf{P}}(\tilde{\mathbf{\Lambda}}^{+} + \tilde{\mathbf{\Lambda}}^{-})\tilde{\mathbf{P}}^{-1}\Delta\mathbf{U} \tag{20}$$

where $\mathbf{\Lambda}^{\pm} = (\mathbf{\Lambda} \pm |\mathbf{\Lambda}|)/2$, and the previous decomposition represents the splitting of the gradient in left and right travelling parts. For the updating of a single cell, only the in-going contributions are taken into account so that the contour integral of the numerical normal flux is equivalent to the sum of these waves.

$$\mathbf{U}_i^{n+1} = \mathbf{U}_i^n - \frac{\Delta t}{A_i}\left(\sum_{k=1}^{NE}(\tilde{\mathbf{P}}\tilde{\mathbf{\Lambda}}^{-}\tilde{\mathbf{P}}^{-1}\Delta\mathbf{U})_k\,\mathrm{d}s_k\right)_i^n + \Delta t\,\mathbf{S}_i^{*n} \tag{21}$$

For the numerical source, $\mathbf{S}^*$, an approach of the integral of the source term $\mathbf{S}$ over the cell has to be defined. First, it should be noted that the source term vector can be decomposed in two different parts that will be treated separately: the bottom variations $\mathbf{S}^1$ and the friction term $\mathbf{S}^2$, $\mathbf{S} = \mathbf{S}^1 + \mathbf{S}^2$.

An upwind approach has been adopted to model the bottom variations in order to ensure the best balance with the flux terms at least in steady cases. This procedure was studied in detail by Bermúdez and Vázquez-Cendón [1]. The flux discretization in Equation (21) can be used in the same way for the bottom slope terms because both contemplate the same spatial derivative.

For every cell-edge k of cell Ω_i the discrete source term is decomposed into inward and outward contributions

$$\tilde{\mathbf{S}}_k^1 = \tilde{\mathbf{S}}_k^{1+} + \tilde{\mathbf{S}}_k^{1-}$$

being

$$\tilde{\mathbf{S}}_k^{1\pm} = \tilde{\mathbf{P}}(\mathbf{I} \pm |\tilde{\mathbf{\Lambda}}|\tilde{\mathbf{\Lambda}}^{-1})\tilde{\mathbf{P}}^{-1}\tilde{\mathbf{S}}_k^1 = \sum_{m=1}^{3}\beta^{m\pm}\tilde{\mathbf{e}}^m \tag{22}$$

The average value $\tilde{\mathbf{S}}_k^1$ computed with

$$\tilde{\mathbf{S}}_k^1 = \begin{pmatrix} 0 \\ g\tilde{h}\Delta z_x \\ g\tilde{h}\Delta z_y \end{pmatrix}_k \tag{23}$$

where $\tilde{h}$ consists of the average obtained from the depth values stored in the left and right cell that share the same edge in each computational cell:

$$\tilde{h} = \frac{1}{2}(h_R + h_L) \tag{24}$$

and the bed increments in each direction are computed in the form

$$\Delta z_x = -(z_R - z_L)n_x, \quad \Delta z_y = -(z_R - z_L)n_y, \quad \mathbf{n} = (n_x, n_y) \tag{25}$$

For every cell Ω_i the total contribution of the source terms is made of the sum of the parts associated to inward normal velocity at every edge k

$$\tilde{\mathbf{S}}_i^{1*} = \sum_{k=1}^{NE} \tilde{\mathbf{S}}_k^{1-}$$

For that reason we define the numerical source term at cell-edge k as

$$\mathbf{S}_k^{1*} = \tilde{\mathbf{S}}_k^{1-}$$

The expressions for the β^- coefficients are

$$\left.\begin{aligned} \beta^{1-} &= \frac{1}{2\tilde{c}}\left(1 - \frac{|\lambda_1|}{\lambda_1}\right)(\mathbf{S}_2{}^1 n_x + \mathbf{S}_3{}^1 n_y) \\ \beta^{2-} &= \frac{1}{\tilde{c}}\left(1 - \frac{|\lambda_2|}{\lambda_2}\right)(-\mathbf{S}_2{}^1 n_y + \mathbf{S}_3{}^1 n_x) \\ \beta^{3-} &= \frac{-1}{2\tilde{c}}\left(1 - \frac{|\lambda_3|}{\lambda_3}\right)(\mathbf{S}_2{}^1 n_x + \mathbf{S}_3{}^1 n_y) \end{aligned}\right\} \tag{26}$$

The average value, Equation (23), proposed in Bermúdez *et al.* [2] ensures a conservative discretization of this source term. The friction term $\mathbf{S}^2$ is discretized in a pointwise manner

$$\mathbf{S}_i^{2*} = (\mathbf{S}_i^2)^n \tag{27}$$

so that the final expression for the numerical scheme is

$$\mathbf{U}_i^{n+1} = \mathbf{U}_i^n - \frac{\Delta t}{A_i}\left(\sum_{k=1}^{NE}(\mathbf{E}_k^* \cdot \mathbf{n}_k \, \mathrm{d}s_k - A_i \mathbf{S}_k^{1*})\right)_i^n + \Delta t(\mathbf{S}^2)_i^n \tag{28}$$

The stability criterion adopted has followed the usual in explicit finite volumes [17] for the homogeneous system of equations not including source terms. In practice, some restrictions on the CFL can be observed due to the non-linearity of the system of equations or to the presence of source terms. Theoretical studies on this question are still in development.

4. DOMAIN BOUNDARIES

The procedure described in the previous section is applied for the ordinary cells, that is, those representing points at the interior of the wetted domain. The boundaries of the wetted domain are defined by the cells not completely surrounded by other cells. All these cells actually require the definition of suitable boundary conditions in order to reach the solution of a problem. However, for transient flows a distinction can be made considering either wetted domains fixed in extension, that is, limited by vertical walls, or those whose size changes as time progresses, that is, those involving sloping walls and moving boundaries.

In this work, boundary conditions are, strictly speaking, applied only at fixed boundaries. The moving boundaries are considered as wetting fronts and hence included in the ordinary cell procedure in a through calculation that assumes zero water depth for the dry cells. This approach provides satisfactory results when dealing with wetting fronts over flat or downward

sloping surfaces but can lead to difficulties in advances over adverse slopes. This is what is called in this work the wetting/drying front. The procedure followed both for boundary conditions and for wetting/drying fronts is next outlined.

4.1. Boundary conditions

As in any other boundary problem in computational fluid dynamics, there is first a question concerning the number of physical boundary conditions required at every boundary point. To help, the theory of characteristics in 2D tells us that, depending on both the value of the normal velocity through the boundary

$$\mathbf{u} \cdot \mathbf{n} = un_x + vn_y \tag{29}$$

and the local Froude number $Fr = (\mathbf{u} \cdot \mathbf{n})/c$, there are four possibilities as detailed in Hirsch [5]:

(i) Supercritical inflow: $\mathbf{u} \cdot \mathbf{n} \leqslant -c \Rightarrow$ all the variables must be imposed.
(ii) Subcritical inflow: $-c < \mathbf{u} \cdot \mathbf{n} \leqslant 0 \Rightarrow$ two variables must be imposed.
(iii) Supercritical outflow: $\mathbf{u} \cdot \mathbf{n} > c \Rightarrow$ none of the variables must be imposed.
(iv) Subcritical outflow: $0 < \mathbf{u} \cdot \mathbf{n} \leqslant c \Rightarrow$ one variable must be imposed.

A second question is related to the procedure used to obtain numerical boundary conditions [5]. In the work presented here, the idea of using a Riemann solver to calculate the flux at the edges of a cell has also been used at the boundaries. The variables are stored at the center of each cell and the boundary conditions are also imposed there, in boundary cells. The value of the variables not prescribed is calculated from a usual finite volume balance. For this purpose, the fluxes across the edges lying on the boundary are estimated by means of a 'ghost' outside cell. Usually, the ghost cell just duplicates the boundary cell. When the boundary is a solid wall, the ghost cell is a mirror cell in which the depth of water has the same value as the boundary cell and the velocities have the opposite sign. Specific values of the input boundary conditions in each case are detailed in Section 5. In all the examples presented, the domain is closed almost everywhere. At the outflow points, a free flow condition is assumed and this is modelled by means of a supercritical-type boundary condition.

4.2. Wetting/drying fronts

The wetting front advance over a dry bed is a moving boundary problem in the context of a depth averaged two-dimensional model. As such, the optimum way to deal with it is to find the physical law that best defines the dynamics of the advancing front to use it as the physical boundary condition to be plugged into the above procedure. The question about that physical law makes us reconsider the 3D basic equations at the wetting front position. In advance over adverse dry bed the water column tends to zero smoothly and, hence, the free surface and bottom level tend to reduce to one point where both the free surface and bottom boundary conditions apply simultaneously [18]. This line of reasoning, being interesting, does not solve the discrete problem in a simple way but, on the contrary, leads to the generation of an alternative technique for a number of cells that increases in time as the wetting progresses.

In a different approach closer to the discrete solution, wetting fronts over dry surfaces can be reduced to Riemann problems in which one of the initial depths is zero. This problem can be analytically studied for simplified conditions and the solution exists both for horizontal

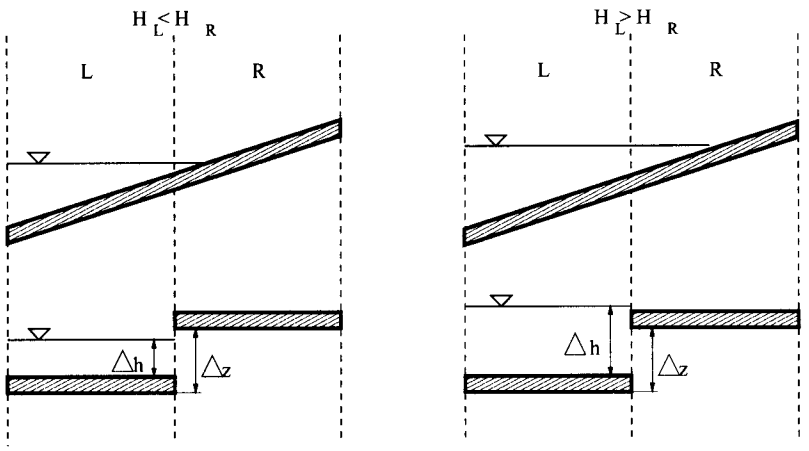

Figure 1. Steady wetting/drying fronts over adverse steep slopes in real and discrete representations.

bed (Ritter solution) [19] and for sloping bed [20]. The solution in the latter case, when dealing with adverse slopes, identifies a subset of conditions incompatible with fluid motion (stopping flow). On the other hand, the numerical technique described in Section 3 is an approximate Riemann solver adapted to cope with zero depth cells which provides a discrete solution to the problem in all these cases not identifying correctly the stopping flow conditions. Therefore, this technique is unable to solve correctly situations of still water in a domain of irregular shape, generating spurious velocities in the wet/dry contour and often violating mass conservation.

Previous works on this topic have reached this point and some authors working with finite elements solve the problem allowing the controlled use of negative depths [21–23]. In finite volumes, in an attempt to blend the two points of view generating at the same time a simple and efficient rule for this situation, the following steps are proposed. In the upper part of Figure 1 water and bottom surface are plotted and at the lower part their discrete representation with constant functions z and H over the cells. First of all, and with reference to Figure 1, the variable $H = h + z$ is compared between any two cells defining a wetting front over adverse slope and two situations can be found:

(i) $H_L < H_R$. This corresponds to the stopping conditions and hence something has to be done to modify the basic procedure.
(ii) $H_L \geqslant H_R$. Nothing has to be done. The basic Riemann solver in the numerical scheme provides a satisfactory solution.

Some authors propose a solid wall treatment in the case $H_L < H_R$ [24, 25]. This option does not prove optimal since imposing zero velocity does not guarantee that the first equation (mass equation) is fulfilled generating inaccurate jumps in water depth. Instead, an alternative is adapted here forcing the mass balance by means of a modification of the bed slope. For the sake of simplicity in the discussion, let us consider a one-dimensional case of still water ($u = v = 0$). With reference to Figure 2, assume that the stopping condition occurs at the cell interface LR. It can be seen following Bermúdez *et al.* [2] that the discretization of the mass equation to ensure still water steady state at the interface LR, that is, the flux and source

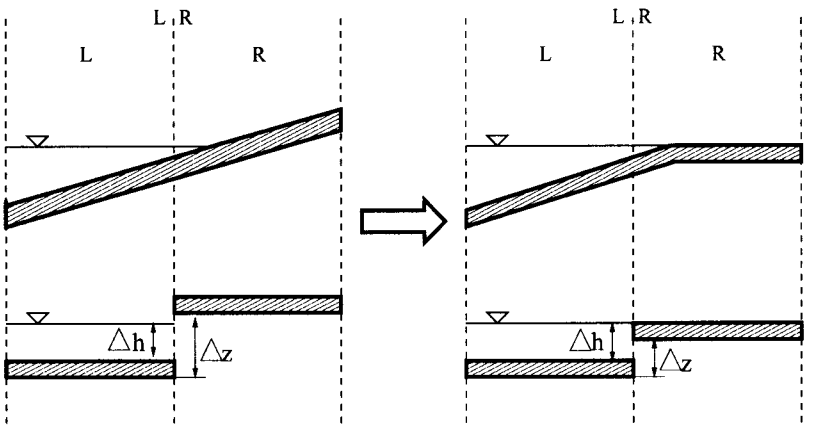

Figure 2. Modification of the bed slope in steady wetting/drying fronts over adverse steep slopes in real and discrete representations.

discretizations must balance:

$$-\frac{\Delta t}{A_i}\left(\sum_{k=1}^{NE}(\mathbf{E}_k^* \cdot \mathbf{n}_k \, \mathrm{d}s_k - A_i \mathbf{S}_k^{1*})\right)_i^n + \Delta t(\mathbf{S}^2)_i^n = 0 \tag{30}$$

This balance leads to the equilibrium condition:

$$(\Delta H)_{LR} = 0 \Rightarrow (\Delta z)_{LR} = -(\Delta h)_{LR} \tag{31}$$

This condition is not always fulfilled due to the piecewise constant representation of the variables in which the bottom level and water depth are stored at the centre of the cells in the numerical model. At the interface LR (Figure 2) a situation is possible in which $(\Delta z)_{LR} \neq -(\Delta h)_{LR}$ leading to numerical velocities without physical meaning (Figure 10). The steady flow problem is converted into an unsteady one producing movement in water that should be always at steady state and mass conservation is lost.

The above requirement (Equation (31)) can also be written

$$h_R - h_L = z_L - z_R \Rightarrow h_R = h_L - (z_R - z_L) < 0$$

thus predicting the appearance of negative depths at the outside of the wetted domain. In a different approach, and in order to avoid the numerical error, the technique proposed here is to enforce the local redefinition of the bottom level difference at the interface to fulfil the equilibrium condition (31) and therefore mass conservation (Figure 2 right):

$$z_R^{\mathrm{mod}} = z_L - (h_R - h_L) \;\Leftrightarrow\; (\Delta z)_{RL}^{\mathrm{mod}} = -(h_R - h_L) \tag{32}$$

In unsteady cases, i.e., for wetting fronts advancing over an adverse dry slope, the procedure followed is the same. However, in this case the numerical representation of the slope between the two adjacent cells may produce a too rapid propagation of the front. It is necessary to reduce to zero the velocity components u, v at the interface LR; otherwise some water could easily jump to the dry upper cell.

5. APPLICATIONS

5.1. Simulation of a tidal wave over an adverse not constant slope

The first example is a test proposed by Heniche *et al.* [21]. It reproduces the movement driven by a tidal wave into the variable slope shoreline in a rectangular channel. The length of the channel is 500 m and the width 25 m. The bed slope in the x direction is: -0.001 in the first 100 m, -0.01 between 100 m and 200 m and -0.001 between 200 m and 500 m of the reach of the channel. It is assumed horizontal in the y direction. A steady state with $H = 1.75$ m of quiescent water depth is considered as the initial condition. The fixed boundaries are solid walls except the inlet located at $x = 500$ m. Inflow boundary conditions are associated with the variation of the water depth in time with the tidal wave in the form

$$h(500, t) = h_0 + \eta \cos\left(2\pi \frac{t}{T}\right) \tag{33}$$

where $h_0 = 1$ m is the reference water level, $\eta = 0.75$ m is the amplitude of the tidal wave and $T = 60$ min is the period of the cycle. The physical domain has been discretized with constant intervals $\Delta x = 5$ m. The Manning roughness coefficient takes the value $n = 0.03$.

In Figure 3 the differences in the solution of the water depth when using or not the wetting–drying condition proposed here are shown. For this purpose, a representation of the water depth

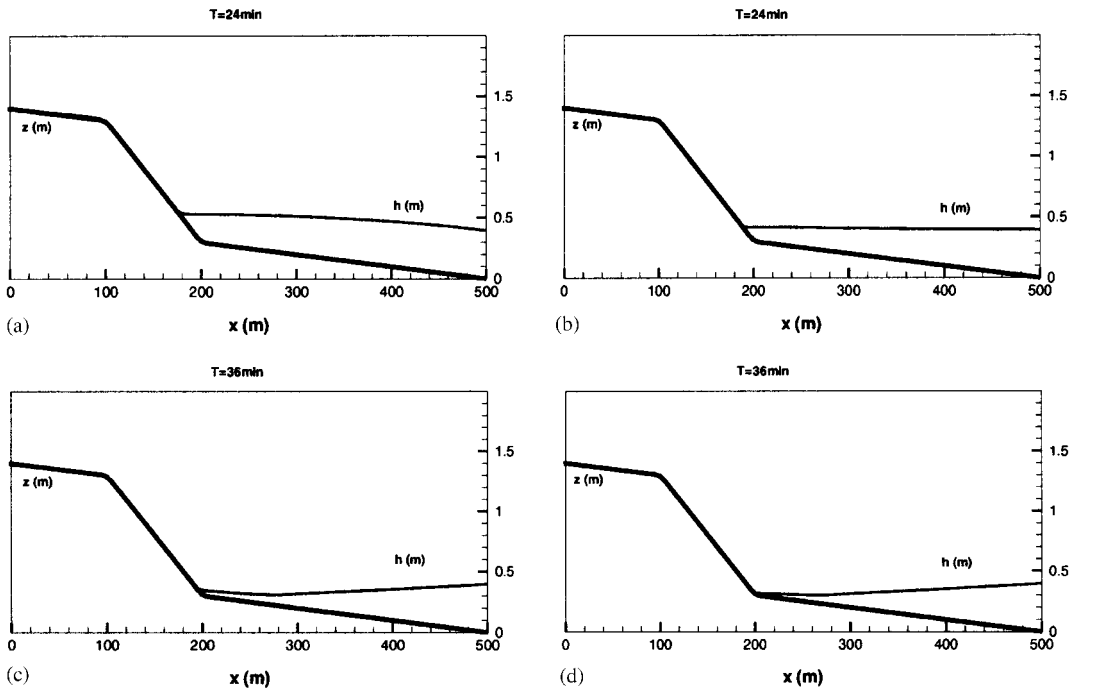

Figure 3. Water depth at time $T = 24$ min (a, b) and $T = 36$ min (c, d) over the bed slope when the wetting–drying condition is not used (a, c) and when it is used (b, d) in the simulation of a tidal wave over an adverse, not constant, slope. Coarse line represents bottom surface and fine line free surface.

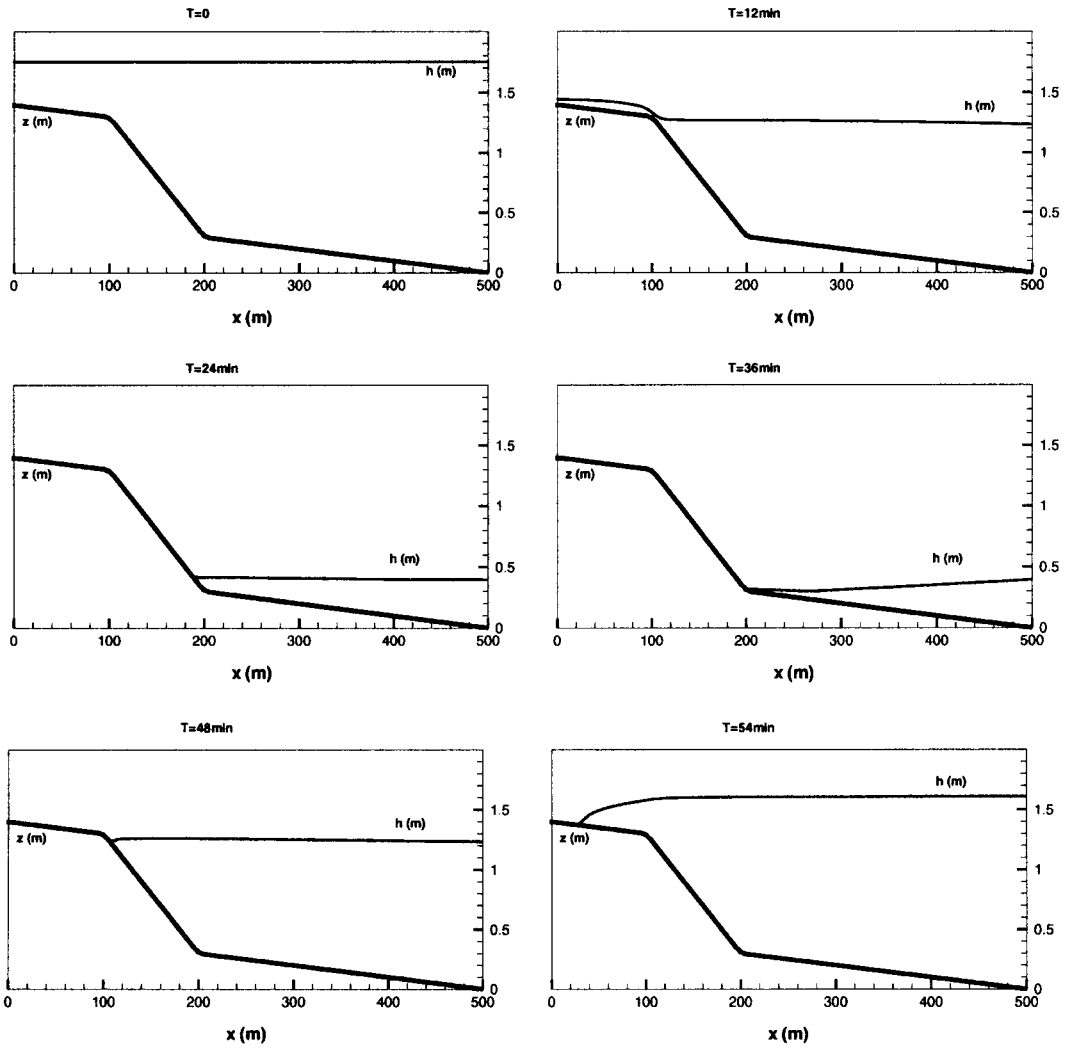

Figure 4. Snapshots of the advance/recession of the wetting/drying front over the bottom at time: $T = 0, 12, 24, 36, 48$ and 54 min in the simulation of a tidal wave over an adverse not constant slope.

at time $T = 24$ min and $T = 36$ min when the wetting–drying condition is not used (a,c) and when it is used (b,d) is presented. In Figure 4 a set of profiles showing the time evolution of the advance/recession of the wetting/drying front caused by the tidal wave over the adverse variable slope is presented. These results, using the wetting/drying condition proposed here, can be seen to compare favourably with those obtained by Heniche *et al.* [21] who use a completely different technique based on finite element methods.

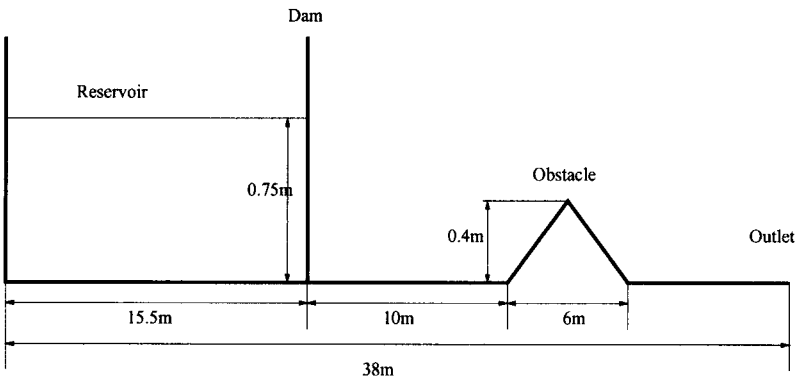

Figure 5. Geometry of the experimental model in the simulation of a dam break and advance over a triangular obstacle.

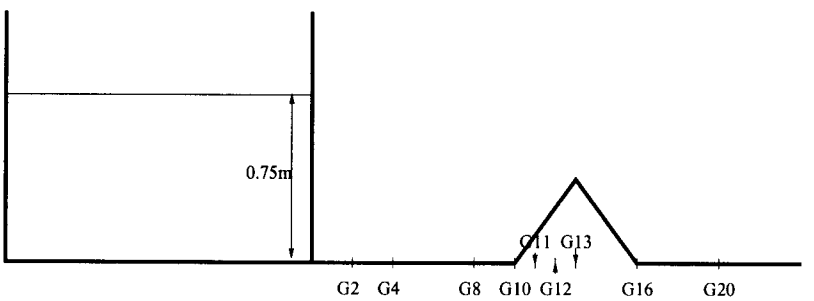

Figure 6. Location of the gauging points in the experimental model for the simulation of a dam break and advance over a triangular obstacle.

5.2. Dam break and advance over a triangular obstacle

In the second example, numerical results are compared with experimental data obtained from the Recherches Hydrauliques Lab. Châtelet together with the University of Bruxelles (Belgium) under the supervision of J.M. Hiver. The test case deals with the evolution of a dam-break wave over a triangular obstacle. The channel geometry is presented in Figure 5. The physical model combines a reservoir connected to a rectangular channel. The length of the entire model is 22.5 m. The dam is situated at $x = 15.5$ m. A triangular obstacle (6 m long, 0.4 m high) is situated 13 m downstream the dam over the bed of the channel. The slopes of the obstacle are symmetric. The initial conditions considered are 0.75 m of water depth in the reservoir and dry bed in the rest of the channel. The fixed boundaries are solid walls except for the free outlet. The Manning roughness coefficient is 0.0125 for the bed and 0.011 for the vertical walls of the rectangular channel, values supplied by the experimentalists from a steady flow test case.

The predicted and measured water depth time evolution during 40 s at the gauging points (Figure 6) situated in: G4 at 4 m, G10 at 10 m, G11 at 11 m, G13 at 13 m and G20 at 20 m are shown in (Figure 7). The next figure (Figure 8) compares the numerical results obtained

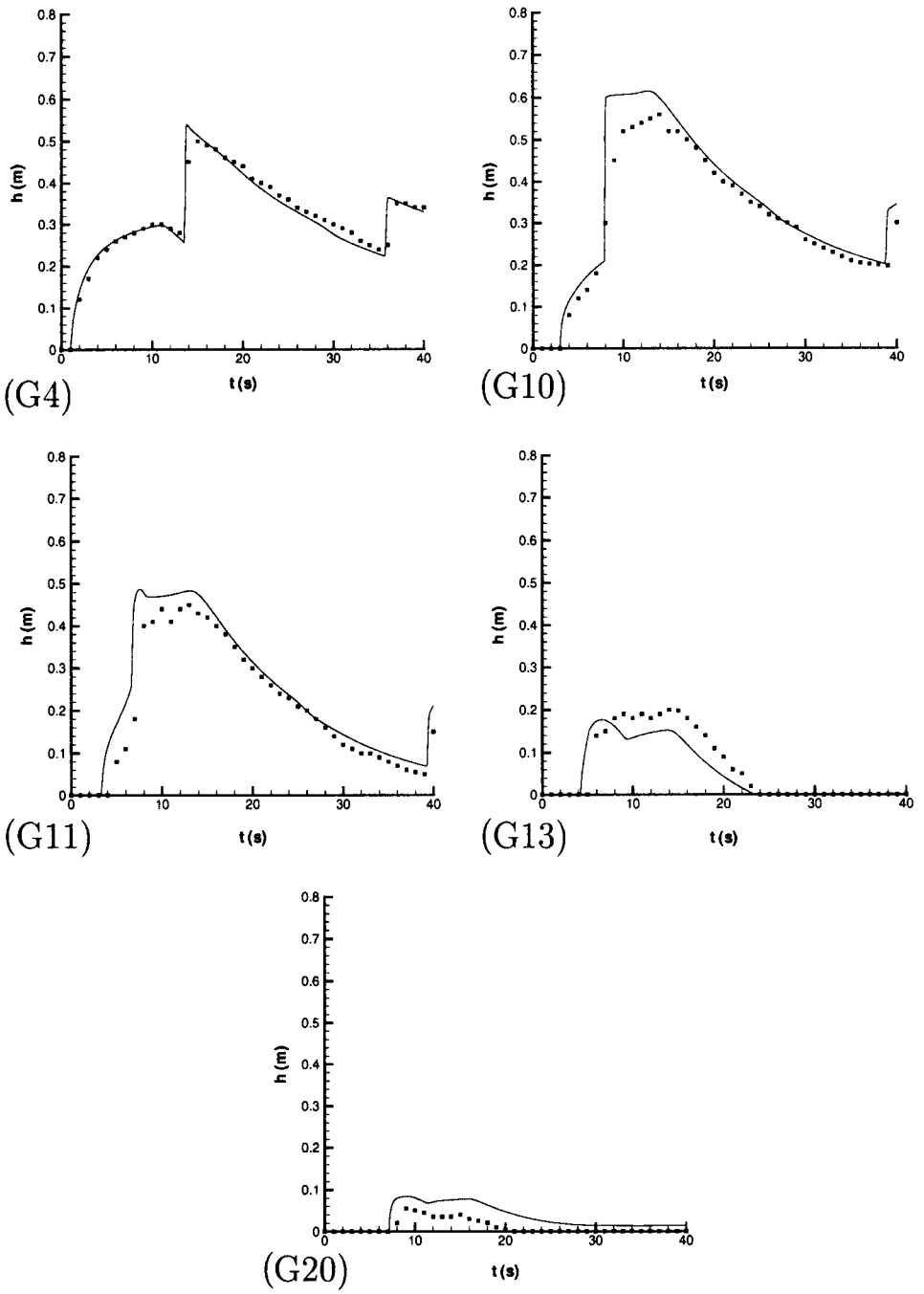

Figure 7. Time evolution during 40 s of the water depth measured and computed at gauging points: G4, G10, G11, G13 and G20 in the simulation of a dam break and advance over a triangular obstacle. Points stand for experimental measures and solid line for numerical results.

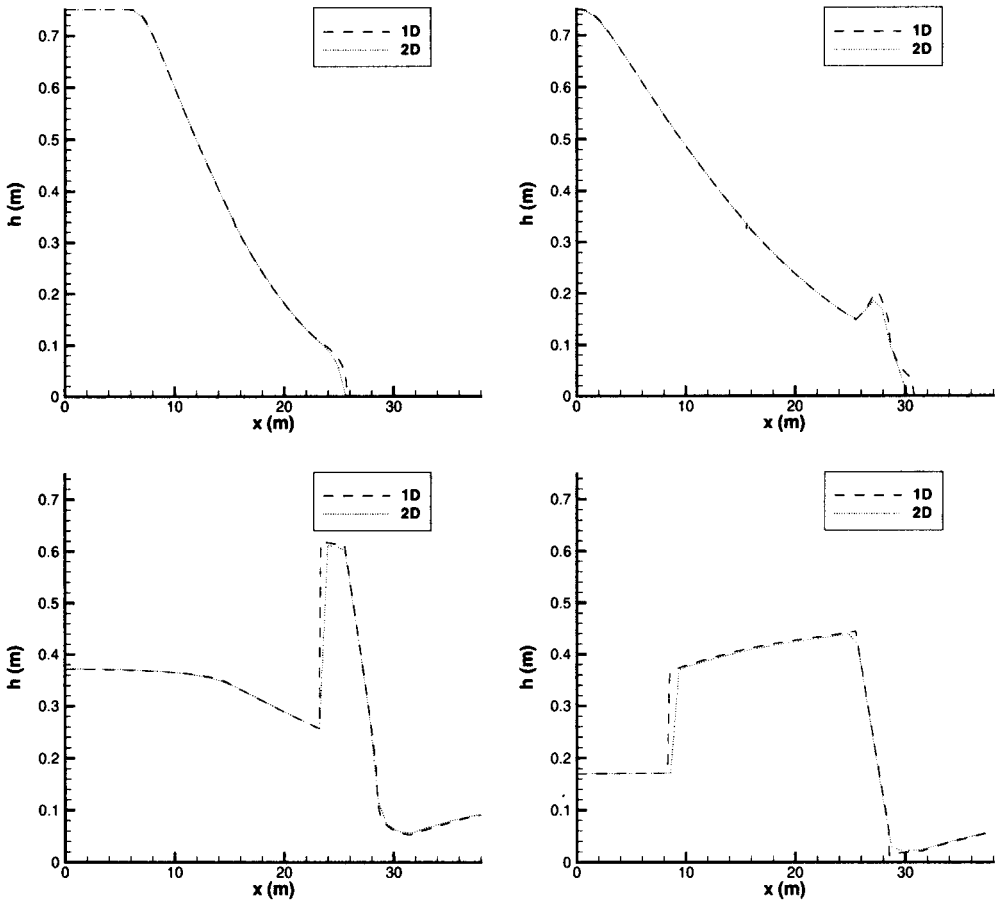

Figure 8. Numerical results obtained with a 1D and a 2D scheme on the water depth profiles along the channel at times: $T = 3, 5, 10$ and 20 s in the simulation of a dam break and advance over a triangular obstacle.

for the water depth at different times $T = 3\,\text{s}, 5\,\text{s}, 10\,\text{s}$ and 20 s from the 1D and 2D numerical schemes to check the coherence of both schemes. The coincidence of the numerical results obtained with both schemes can be observed, as expected, due to the marked one-dimensional character of the flow. Comparisons of numerical results using or not the wetting/drying condition are not shown in the figures because the differences were insignificant. The concordance between the experimental and numerical results is also satisfactory. At the gauging points located before the obstacle, the prediction of the arrival time of the wave as well as the water depth is good. Point $G13$ is located at the vertex of the obstacle and therefore is a critical point. It can be observed that the prediction of the transitions from wet to dry is correct. At the last point we can observe a little disagreement between measures and numerical results but the amount of water is insignificant.

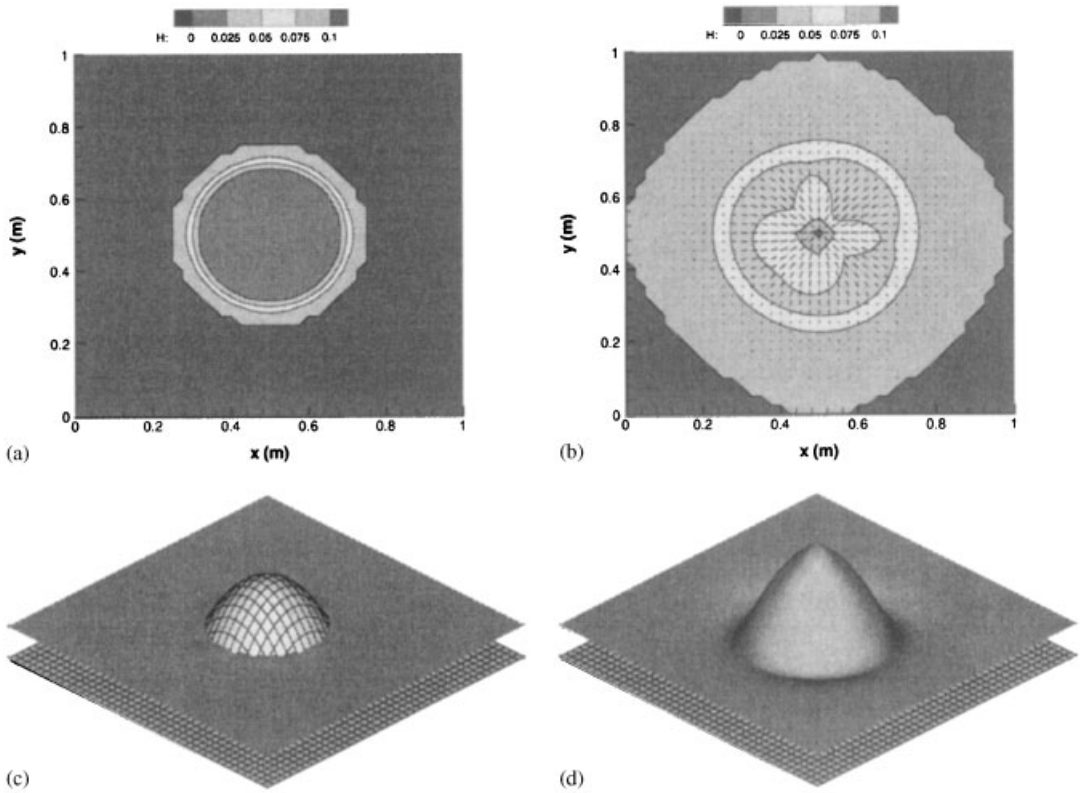

Figure 9. Iso-contour water levels and velocity field (a, b) and free surface (c, d) of steady state in a closed pool with a partially covered bump using an upwind (a, c) and a pointwise (b, d) discretization in the propagation of a smooth wave over a bump test case.

5.3. *Propagation of a smooth wave over a bump*

The numerical experiment takes place in a square pool $1\ \mathrm{m} \times 1\ \mathrm{m}$. At the centre of the pool a symmetric bump in the bottom is mathematically defined in the form

$$z(x, y) = \max\left[0., 0.25 - 5 * \left(\left(x - \frac{1}{2}\right)^2 + \left(y - \frac{1}{2}\right)^2\right)\right] \tag{34}$$

The ability of the method to preserve the initial steady state in time is analysed. We start from still water as the initial condition covering partially the bump in a frictionless domain fully closed by vertical walls.

$$H = 0.1\ \mathrm{m}, \quad u = 0\ \mathrm{m\ s^{-1}}, \quad v = 0\ \mathrm{m\ s^{-1}} \tag{35}$$

Figure 9 shows the numerical results when the bed slope is discretized with a pointwise (central) or with an upwind discretization using the wetting/drying condition proposed in Section 4.2. The mesh used is the same for both cases with 1600 quadrilateral cells. Once

initial still water conditions are specified, the steady state must be conserved. If the bed slope discretization has been correctly made no change in the free surface or in the velocity field (always zero) must be observed, because there are no external forces that could produce any movement. The upper figures in Figure 9 show the iso-contour water levels together with the velocity field. The lower figures show the free surface. On the left the results obtained with the upwind discretization using the wetting/drying condition are shown and on the right the same results using a pointwise approximation for the bed slope source terms are represented.

The differences are obvious. It is significant how the initial value of the velocity components is conserved in case of using the upwind discretization because the initial state is conserved exactly while spurious velocities appear; they originated from the numerical approximation, when a pointwise discretization for the bed slope is used. The necessity of upwinding the source terms corresponding to the bottom variations is noted here and not doing so can lead to important numerical errors. With this discretization *Property-C* defined in References [1] and [2] for the one and two dimensional cases respectively, is verified also in the steady wetting/drying front.

Next, assuming the necessity of an upwind discretization of the bottom variation, the influence of the wetting–drying condition alone is studied. The upper plots in Figure 10 show the iso-contour water levels together with the velocity field. Lower figures show the free surface. On the left the results are obtained using the wetting–drying condition stated in Section 4.2 while on the right no special wetting–drying condition is used. It can be seen that water easily jumps over the bump in the latter case showing that the wetting–drying condition is necessary to preserve the steady state, directly related with mass conservation.

5.4. Non-symmetric dam break in a pool with a pyramidal obstacle

The physical model was built at the Hydraulic Lab. of CITEEC (Spain) under the super vision of J. Puertas. The model consists of a closed pool separated in two parts by a solid wall where a gate (dam) is located in a non-symmetric place (Figure 11).

The walls surrounding the pool and the wall separation are made of concrete, there is no possibility of outflow and the bed is flat. The experimental–numerical comparison has been chosen among all the experiments carried out with different initial situations. The essay corresponds to the initial depth of water relationship: 0.5/0.1 m. The mesh used is a triangular unstructured one with 2625 cells. The *CFL* condition is 0.8. In Figure 12 experimental data and numerical results are compared on the time evolution of water depth during 20 s at the gauging points: $S0, S1, S2$ around the pyramidal obstacle to check the wetting/drying condition, $P6$, $P7$ and $P18$ in which the propagation of the wave generated by the dam break can be observed.

There exists a small difference on the numerical results in this case of water depth when using or not the wetting/drying condition. The point far from the pyramid, $P18$, is not much affected by the wetting/drying effect over the obstacle and only a curve is included in the plot for clarity. Differences on water depth appear near the obstacle: small peaks of water appear in the first 5 s as can be observed in $S1$. The propagation of the arrival front is well predicted and independent of the wetting/drying condition but both curves (with and without wetting/drying condition) diverge when time evolves.

Analysis of mass conservation has been carried out in this case. Mass conservation errors have been computed taking into account initial mass volume (V_i), final mass volume (V_f) and

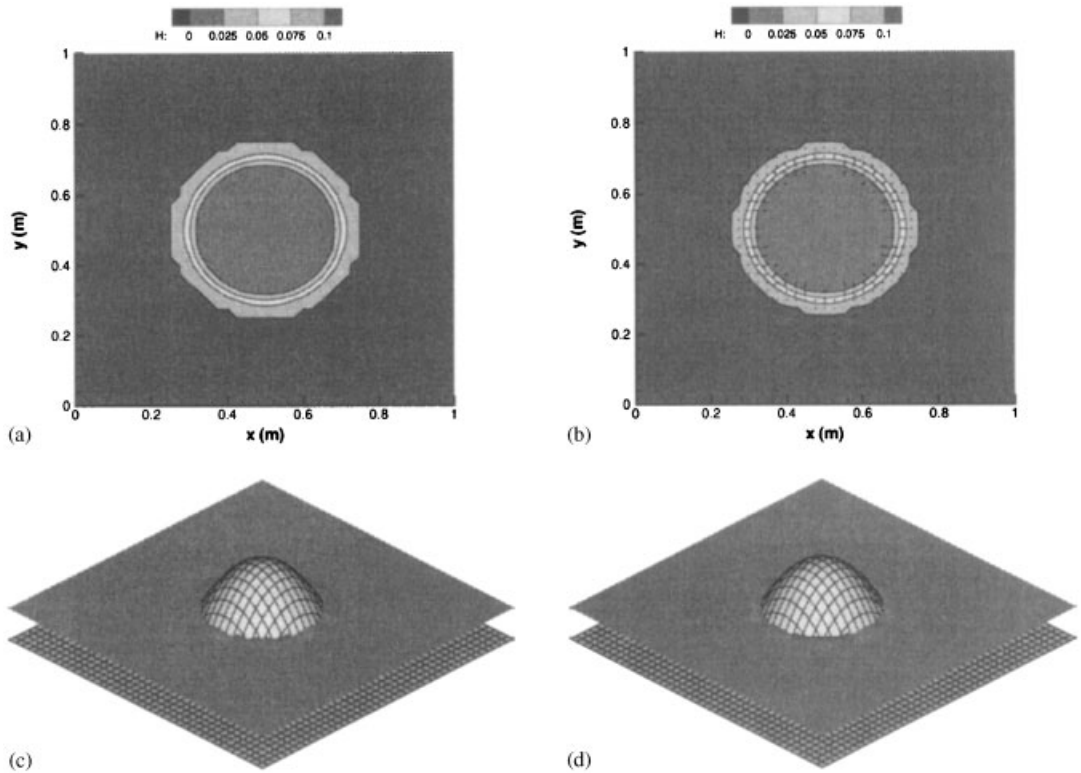

Figure 10. Iso-contour water levels and velocity field (a, b) and free surface (c, d) of steady state in the same test case using (a, c) and not using (b, d) the wetting/drying condition proposed here in the propagation of a smooth wave over a bump test case.

water inflow discharge volume (QI) in the form

$$\text{mass error } (\%) = \frac{V_i + QI - V_f}{V_i + QI} \tag{36}$$

A comparison of the time evolution of mass error using or not the wetting–drying condition proposed in Section 4.2 is shown in Figure 13.

5.5. *Dam break on a channel with three mounds on its bottom*

In this test case, the treatment of moving boundaries separating wetting from drying zones is validated in the simulation of a flow generated by a dam break through a channel which contains three mounds on its bottom as proposed by Kawahara and Umetsu [22]. Figure 14 shows the bottom levels in terms of contour and bottom surface plots together with the geometry of the channel.

The length of the channel is 75 m and its width 30 m. Boundary fixed conditions are solid walls. Initial conditions are those of dry bed. The dam is situated at $x = 16$ m containing 900 m^3 of water. A mesh discretization with 1744 triangular unstructured cells is used. The

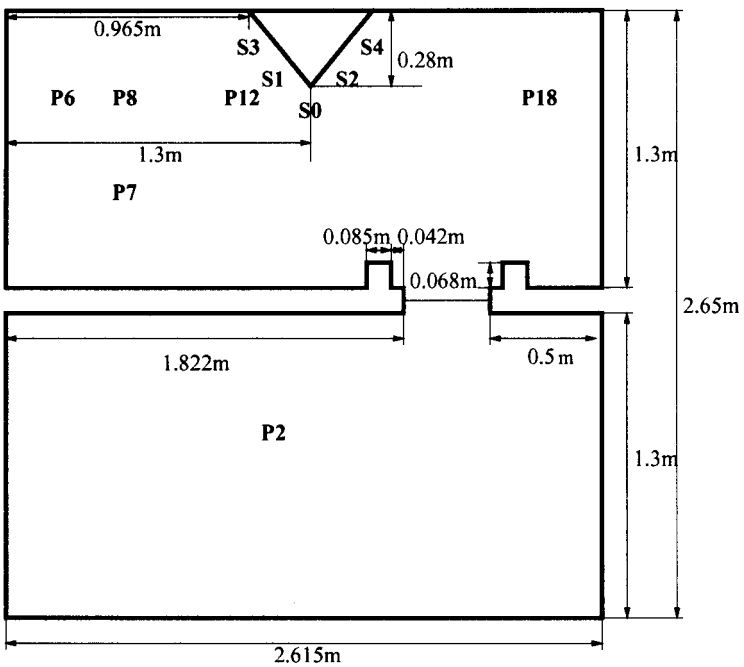

Figure 11. Plane view of the physical model which simulates a non-symmetric dam break in a pool with a pyramidal obstacle.

Manning coefficient is 0.018. Numerical results are represented in Figure 15 where water depth iso-contours, velocity field and free surface over the bottom are represented at different times $T = 2, 6, 12$ and 300 s to show the propagation of the flood till steady state is recovered. Mass losses are controlled.

The small mounds are covered by the flow in its propagation and the effect of advancing and recession over the sloppy bed is clear. The higher mound is always dry and the accumulation of water is clearly observed. Symmetry along the flow and the reflected front created by the collision of the advancing front with the mounds is shown. The time evolution of mass error is shown in Figure 16 if no wetting/drying condition is used and when it is used. It can be noticed that mass error values have increased respect to test 5.4, as we can expect because in this case advance takes place over the initially dry bed while in the other case all the pool was initially wet.

5.6. Propagation of a flood wave in the Toce river physical model

In this last test we would like to remark the necessity of including the wetting/drying condition in the computation of floods over irregular geometries. The above tests have demonstrated the differences observed when using or not the technique proposed for wetting/drying fronts in simple cases: smooth bed slopes, low values of Manning roughness coefficient, etc.... In this case, the technique has been applied to the simulation of a flood wave in the Toce river physical model. This model is a simplified one, built in ENEL (Italy), representing

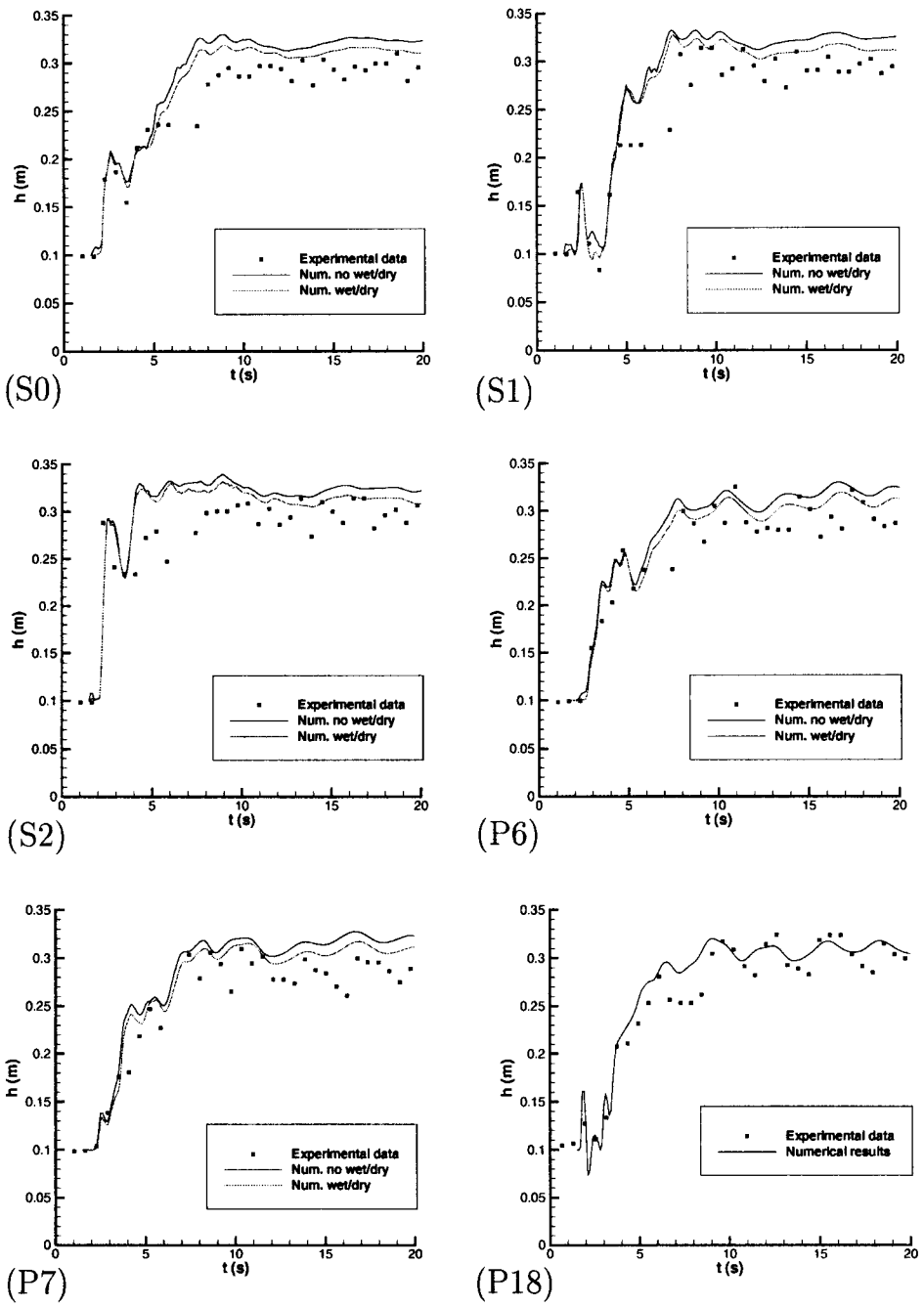

Figure 12. Experimental data and numerical results on the time evolution of water depth during 20s at the measuring points located in Figure 11 in the simulation of a non-symmetric dam break in a pool with a pyramidal obstacle.

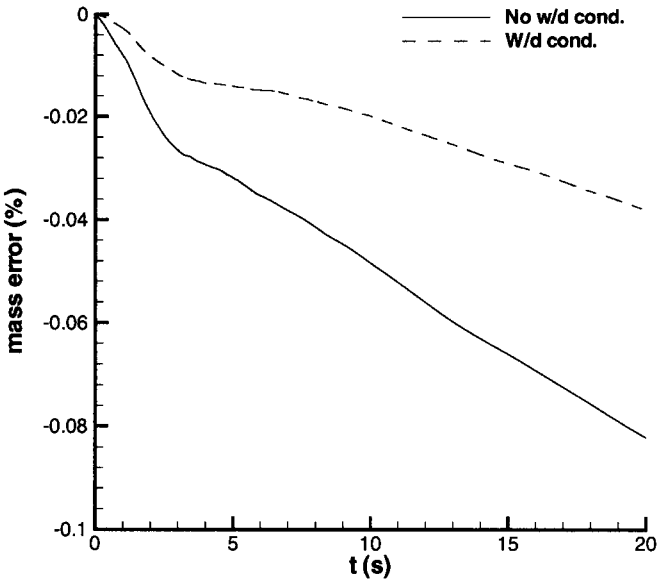

Figure 13. Time evolution during 20 s of mass error using or not the wetting/drying condition in the simulation of a non-symmetric dam break in a pool with a pyramidal obstacle.

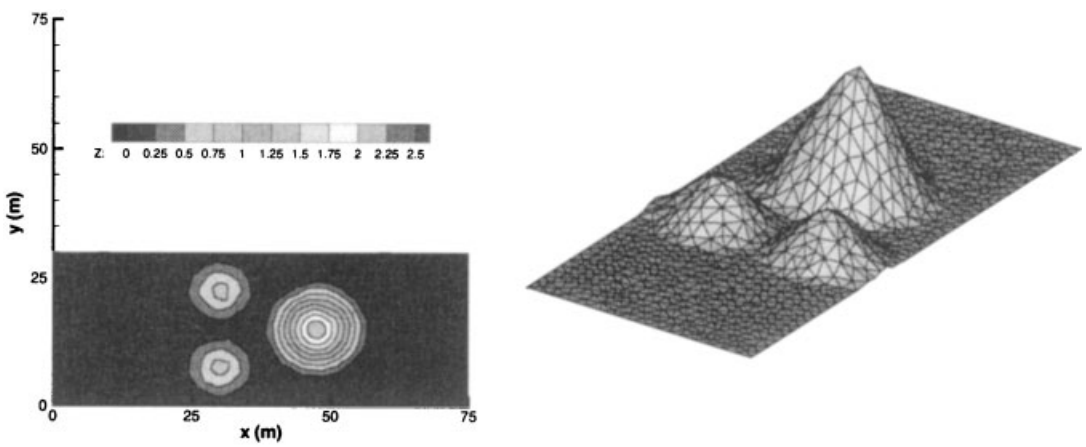

Figure 14. Geometry of the test in iso-contour and free surface representation of the bottom which involves a dam break simulation on a channel with three mounds on its bottom.

the first 5 km reach of the Toce river, located in the Northern Italian Alps. The length scale of the model is 1:100 and the total area of the experimental facility is 55×13 m. It reproduces many details of the real topography such as river bed, an empty reservoir located half reach of the total length of the model. This reservoir represents a big obstacle which causes the flow to bend round it and enter in it after reaching its height. The flood wave is

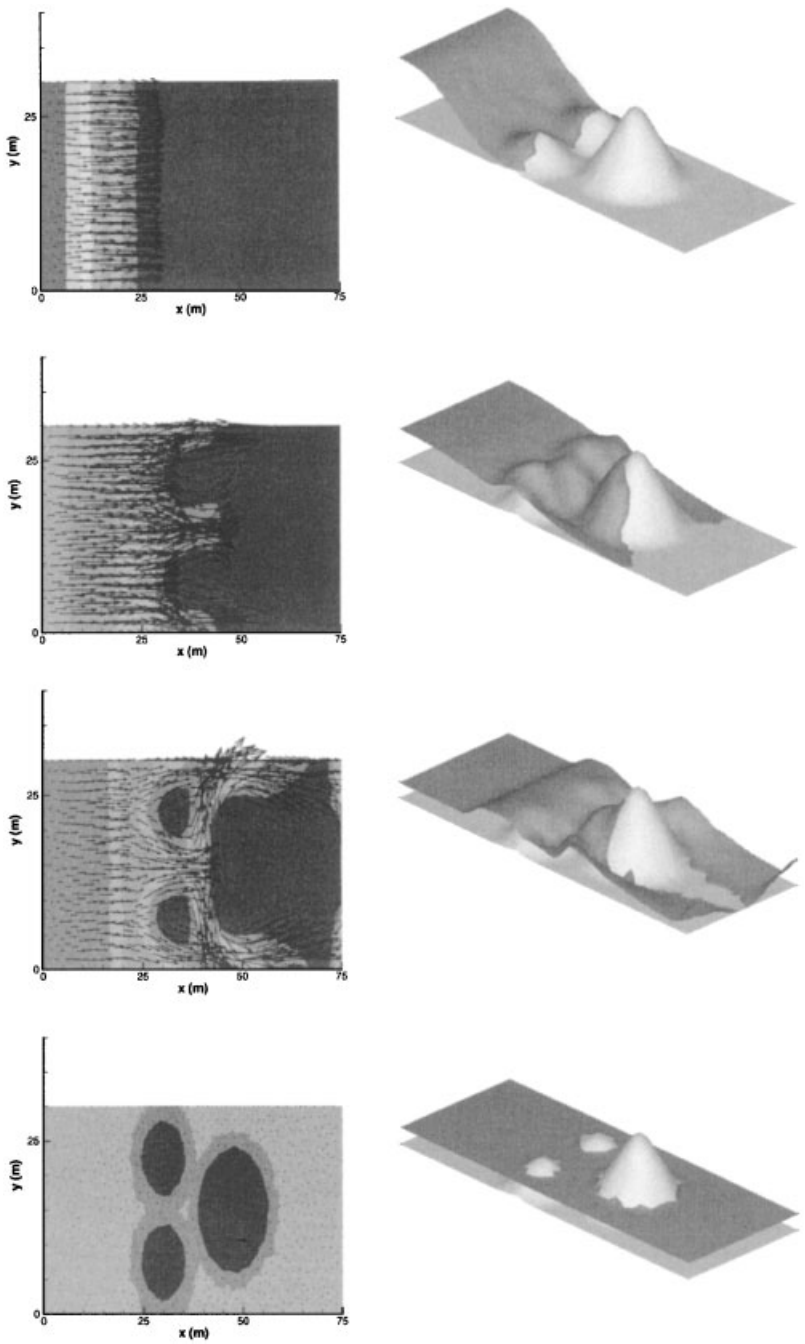

Figure 15. Propagation of water depth over the mounds provoked by a dam break in iso-contour, velocity field and free surface representation at times: $T = 2, 6, 12$ and 300 s.

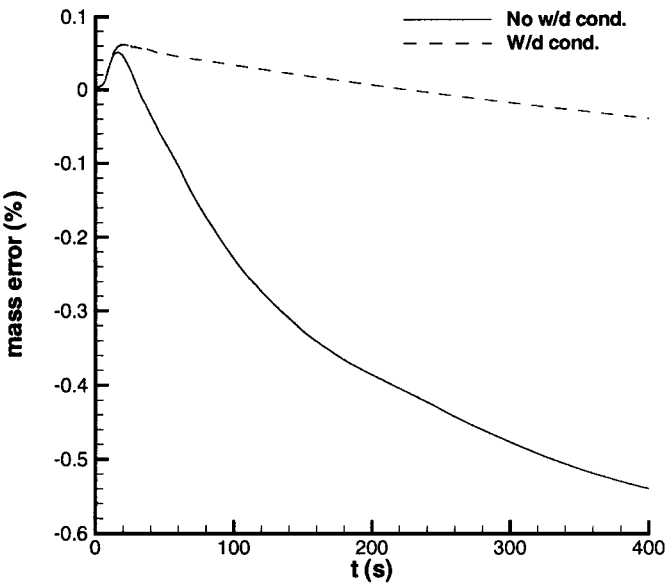

Figure 16. Time evolution during 400 s of mass error using or not the wetting/drying condition in the simulation of a dam break on a channel with three mounds on its bottom.

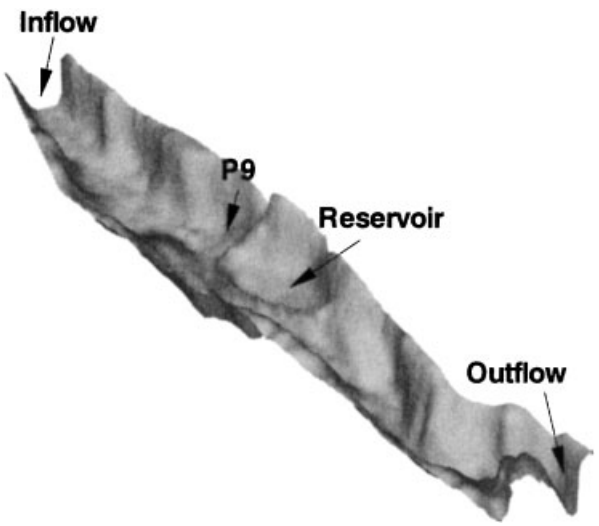

Figure 17. Geometry of the Toce river physical model.

simulated by the abrupt raise of water level contained in an upstream-located tank. Before the computation, an adaptation of the digital geometry supplied by ENEL to the one needed in the numerical unstructured code was carried out by means of a linear interpolation. In Figure 17 the geometry of the model is shown. Boundary upstream conditions are fixed by a

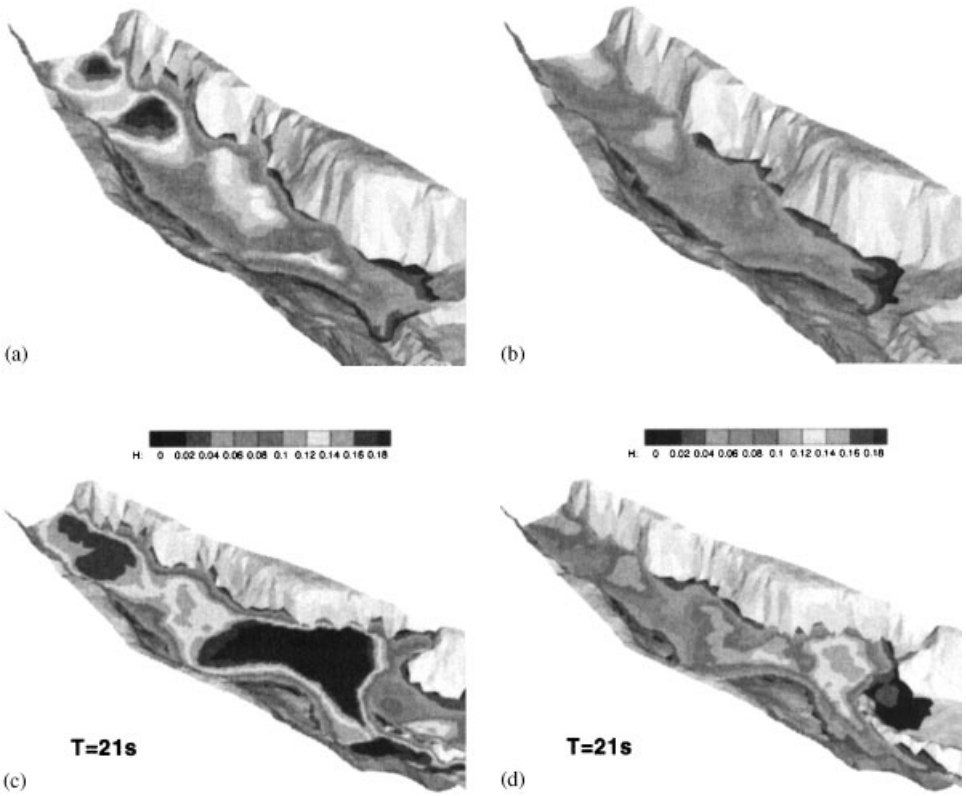

Figure 18. Propagation of a flood wave over the Toce river physical mode at time $T = 12$ (a, b) and 21 s (c, d) when the wetting/drying condition is not used (a, c) and when it is used (b, d).

hydrograph and a limnigraph supplied by ENEL and downstream boundary conditions are let free. The valley remains initially dry. It is worth noting that Manning roughness coefficient is so high ($n = 0.0162$) that an implicit discretization of the friction term was necessary to stabilize the computations.

At the same time the model became flooded, depths of water were measured at selected points in the model. Consistent with the aim of evaluating the performance of the numerical methods, the calculated depths of water at these stations were compared with the experimental ones [26] to know how correctly the flooding was simulated and the amount of confidence that can be put in the predictive capacity of the simulation methods. The general form of the computed–measured depth-time curves agree quite well [26] till the flood passes the reservoir where a bridge is included in the model but not in the simulation. Only one of the figures comparing measured data and numerical results is shown here and the rest can be seen in Brufau [26]. In Figure 18 two comparisons of the flood propagation at two times are shown in iso-contour plots with the same colour scale when the wetting/drying condition is used or not. The differences in time of flood propagation and water depth are clear at the figures leading to mass errors when the wetting/drying condition is not used in the computations. The water level is higher in case the wetting/drying condition is not used, as we could expect from the

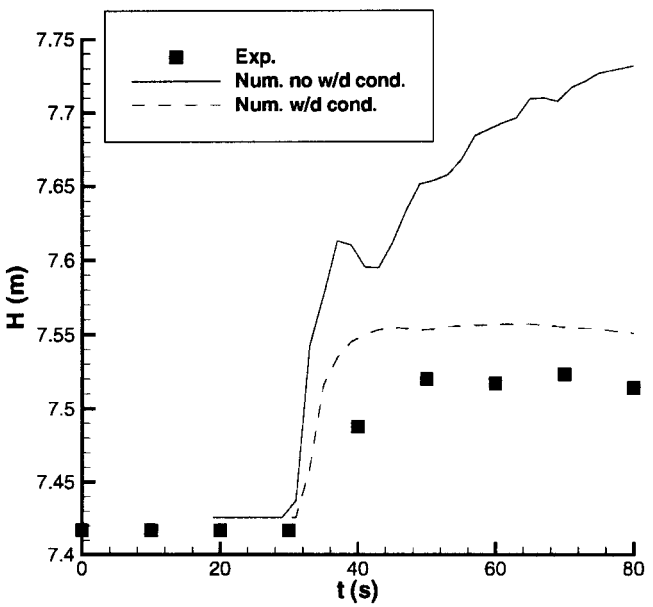

Figure 19. Comparison of experimental and numerical results using or not the wetting/drying condition on the time evolution of the free surface at *P*9 in the Toce river physical model.

other tests. In this simulation, the improvement is clearer due to the irregularity of the bottom and slopes. At 21 s in (d) water is beginning to enter the reservoir while in (c) the reservoir is almost covered because the method is not able to treat the wall surrounding the reservoir correctly and water easily jumps into it. Experimental measures reveal the agreement with numerical results obtained using the wetting/drying condition in the time evolution of water depth at a station installed near the reservoir *P*9 (Figure 19). In Figure 20 time evolution of mass error is compared when the wetting/drying condition is or not used.

6. CONCLUSIONS

A first order upwind scheme has been used to solve one- and two-dimensional problems on steady and unsteady free surface flows. The physical domain has been discretized on structured and unstructured meshes. Source terms representing bed slopes in the equations are determinant in the simulation of flow over irregular geometries. The same upwind approach used on the flux derivatives has been adopted to model the bottom variations to ensure their right balance so as to reproduce steady state exactly. Boundary conditions are divided into fixed and moving. Moving boundaries are considered as wetting fronts and hence included in the ordinary cell procedure in a through calculation that assumes zero water depth for the dry cells. A numerical technique based on the discrete form of the mass conservation equation which guarantees steady state at the wet/dry front has been proposed in this work to avoid difficulties in advances over adverse slopes. Finally, some results have been presented in different situations of steady and unsteady flow to test the performance. A simple modification

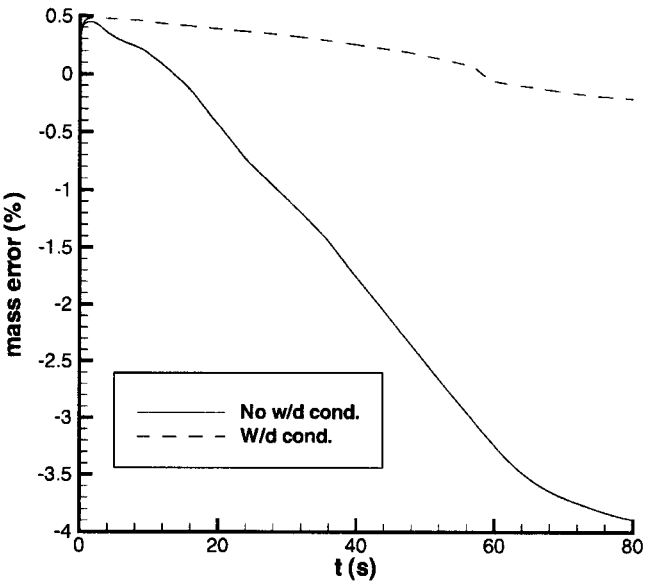

Figure 20. Time evolution during 21 s of mass error using or not the wetting/drying condition on the propagation of a flood wave in the Toce river physical model.

of the basic upwind method improves the numerical solution so that the flow propagation over initially dry bed does not constitute an extra numerical source of error. Instead, it may reduce remarkably the mass conservation error in practical applications such as river flow problems. The numerical technique is validated with the successful comparison between the numerical results and the experimental data as we have shown in some applications.

ACKNOWLEDGEMENTS

The authors would like to thank the Recherches Hydrauliques Lab. Châtelet together with the University of Bruxelles (Belgium), CITEEC (Spain) and ENEL (Italy) for providing experimental data for this research. They would like also to thank the financial support of REN2000-1162-C02-02 MAR.

REFERENCES

1. Bermúdez A, Vázquez ME. Upwind methods for hyperbolic conservation laws with source terms. *Computers and Fluids* 1994; **8**:1049–1071.
2. Bermúdez A, Dervieux A, Desideri JA, Vázquez ME. Upwind schemes for the two-dimensional shallow water equations with variable depth using unstructured meshes. *Computer Methods in Applied Mechanical Engineering* 1998; **155**:49–72.
3. Abbott MB. *Computational Hydraulics*. Ashgate Pub. Comp., 1992.
4. Cunge JA, Holly FM, Verwey A. *Practical Aspects of Computational River Hydraulics*. Pitman: London, U.K., 1980.
5. Hirsch C. *Numerical Computation of Internal and External Flows.* Wiley: New York, 1990; vol. 2.
6. MacCormack RW. Numerical solution of the interaction of a shock wave with a laminar boundary layer. Holt M (ed.), *Proceedings of the Second International Conference on Nonlinear Methods in Fluid Dynamics.* Springer, Berlin, 1971; 151–170.
7. Roe PL. Approximate Riemann solvers, parameter vectors, and difference schemes. *Journal of Computational Physics* 1981; **43**(2):357–372.

8. Roe PL. A basis for upwind differencing of the two-dimensional unsteady Euler equations. *Numerical Methods in Fluid Dynamics II.* Oxford Univ. Press: Oxford, 1986.
9. Alcrudo F, Garcia-Navarro P. Flux difference splitting for 1D open channel flow equations. *International Journal for Numerical Methods in Fluids* 1992; **14**.
10. Glaister P. Approximate Riemann solutions of the shallow water equations. *Journal of Hydraulic Research* 1988; **26**(3):293–306.
11. García-Navarro P, Fras A, Villanueva I. Dam-break flow simulation: some results for one-dimensional models of real cases. *Journal of Hydrology* 1999; **216**:227–247.
12. Vázquez-Cendón ME. Improved treatment of source terms in upwind schemes for the shallow water equations in channels with irregular geometry. *Journal of Computational Physics* 1999; **148**:497–526.
13. Chow VT. *Open Channel Hydraulics*. MacGraw–Hill Book Co. Inc., 1959.
14. García-Navarro P, Vázquez-Cendón ME. On numerical treatment of the source terms in the shallow water equations. *Computers and Fluids* 2000; **29**:951–979.
15. Hubbard ME, García-Navarro P. Flux difference splitting and the balancing of source terms and flux gradients. *Journal of Computational Physics* 2000; **165**:89–125.
16. LeVeque RJ. Balancing source terms and flux gradients in high-resolution Godunov methods: the quasi-steady wave-propagation algorithm. *Journal of Computational Physics* 1998; **146**(1):346–365.
17. Brufau P, García-Navarro P. Two-dimensional dam break flow simulation. *International Journal for Numerical Methods in Fluids* 2000; **33**:35–57.
18. Vreugdenhil CB. *Numerical Methods for Shallow-Water Flow.* Kluwer: Dordrecht, The Netherlands, 1994.
19. Stoker JJ. *Water Waves.* Interscience: New York, 1957.
20. Toro EF. *Riemann Solvers and Numerical Methods for Fluid Dynamics: A Practical Introduction*. Springer-Verlag: Berlin, 1997.
21. Heniche M, Secretan Y, Boudreau P, Leclerc M. A two-dimensional finite element drying–wetting shallow water model for rivers and estuaries. *Advance Water Research* 2000; **23**:359–372.
22. Kawahara M, Umetsu T. Finite element method for moving boundary problems in river flow. *International Journal for Numerical Methods in Fluids* 1986; **6**:365–386.
23. Khan AA. Modelling flow over an initially dry bed. *Journal of Hydraulics Research* 2000; **38**(5):383–389.
24. Bento Franco A. Modelacao computacional e experimental de escoamentos provocados por roturas de barragens. *PhD dissertation*, Univ. Técnica de Lisboa, 1996.
25. Sleigh PA, Berzins M, Gaskell PH, Wright NG. An unstructured finite volume algorithm for predicting flow in rivers and estuaries. *Computers and Fluids* 1997.
26. Brufau P. Simulación bidimensional de flujos hidrodinámicos transitorios en geometrías irregulares. *PhD dissertation*, 2000.

